Local quantification of mesoporous silica microspheres using multiscale electron tomography and lattice Boltzmann simulations

Microporous and Mesoporous Materials 302 (2020) 110243

Contents lists available at ScienceDirect

Microporous and Mesoporous Materials

journal homepage: http://www.elsevier.com/locate/micromeso

Local quantification of mesoporous silica microspheres using multiscale electron tomography and lattice Boltzmann simulations

Andreas J. Fijneman [a,b], Maurits Goudzwaard [a], Arthur D.A. Keizer [a], Paul H.H. Bomans [a], Tobias Gebäck [c], Magnus Palmlöf [b], Michael Persson [b], Joakim Högblom [b], Gijsbertus de With [a], Heiner Friedrich [a,d,*]

[a] Laboratory of Physical Chemistry, and Center for Multiscale Electron Microscopy, Department of Chemical Engineering and Chemistry, Eindhoven University of Technology, Groene Loper 5, 5612 AE, Eindhoven, the Netherlands
[b] Nouryon Pulp and Performance Chemicals AB, Färjevägen 1, SE-455 80, Bohus, Sweden
[c] SuMo Biomaterials VINN Excellence Centre, and Department of Mathematical Sciences, Chalmers University of Technology and Gothenburg University, Chalmers Tvärgata 3, SE-412 96, Göteborg, Sweden
[d] Institute for Complex Molecular Systems, Eindhoven University of Technology, Groene Loper 5, 5612 AE, Eindhoven, the Netherlands

ARTICLE INFO

Keywords:
Quantitative electron tomography
Mesoporous silica
Intraparticle diffusivity
Scanning transmission electron microscopy
Lattice Boltzmann simulations

ABSTRACT

The multiscale pore structure of mesoporous silica microspheres plays an important role for tuning mass transfer kinetics in technological applications such as liquid chromatography. While local analysis of a pore network in such materials has been previously achieved, multiscale quantification of microspheres down to the nanometer scale pore level is still lacking. Here we demonstrate for the first time, by combining low convergence angle scanning transmission electron microscopy tomography (LC-STEM tomography) with image analysis and lattice Boltzmann simulations, that the multiscale pore network of commercial mesoporous silica microspheres can be quantified. This includes comparing the local tortuosity and intraparticle diffusion coefficients between different regions within the same microsphere. The results, spanning more than two orders of magnitude between nanostructures and entire object, are in good agreement with bulk characterization techniques such as nitrogen gas physisorption and add valuable local information for tuning mass transfer behavior (in liquid chromatography or catalysis) on the single microsphere level.

1. Introduction

Electron tomography is a powerful technique to image the three-dimensional (3D) structure of an object with nanometer resolution using a series of two-dimensional (2D) electron micrographs. It is frequently used in the biological, chemical and physical sciences to study the 3D morphology of materials [1–7]. Nanoporous materials in particular have received a great deal of attention over the past years, mainly because of their (potential) application in catalysis or separation processes [8–13]. One example is provided by mesoporous silica microspheres that are used as packing material in high performance liquid chromatography (HPLC) [14]. These particles play an important role in the separation and analysis of a large variety of molecules based on differences in mass transfer properties [15,16]. They are often highly porous and have complex pore networks that extend over multiple length scales, making them difficult to study by (Scanning) Transmission Electron Microscopy ((S)TEM) based 3D imaging approaches. This is on account that particles are often in the micrometer range (2–25 μm), which necessitates cutting of the particles with, e.g., focused-ion beam microscopy or an ultramicrotome, thus not yielding information on the single particle level [17]. Non-destructive characterization of micrometer-sized particles has been done with x-ray microcomputed tomography, but this technique does not have the required resolution to resolve pores which are mostly nanometer-sized [18,19]. A recent approach utilizing low convergence angle (LC) STEM tomography has shown great promise for imaging micrometer thick samples with nanometer resolution [20–23].

When imaging micrometer thick samples by (S)TEM tomography, artifacts may occur as image intensity does not scale linearly with respect to the thickness of the sample [24,25]. This nonlinearity will

* Corresponding author. Laboratory of Physical Chemistry, and Center for Multiscale Electron Microscopy, Department of Chemical Engineering and Chemistry, Eindhoven University of Technology, Groene Loper 5, 5612 AE, Eindhoven, the Netherlands.
E-mail address: h.friedrich@tue.nl (H. Friedrich).

https://doi.org/10.1016/j.micromeso.2020.110243
Received 27 January 2020; Received in revised form 9 March 2020; Accepted 6 April 2020
Available online 16 April 2020

cause gradients in image intensity in the tomographic reconstruction because standard reconstruction algorithms are based on linear models (Fig. S2) [26]. Corrections for this nonlinearity are possible for objects consisting of different chemical composition [25,27] or by correlative approaches [28]. As the mesoporous silica particles consist only of one phase (silicon dioxide) and due to limited capability of correlative approaches, we correct instead for the nonlinearity using the near perfect sphericity of the particles.

Relating the 3D imaging results directly to material performance and material properties on the sub particle scale can provide valuable insight on the relationship between structure and performance and can lead to better models to simulate e.g. mass transfer behavior. A good way to quantify mass transfer is by computing the intraparticle diffusivity of the material using computer simulations. There are several ways of doing so but the approach chosen here is to solve the diffusion equation via the lattice Boltzmann method [29]. This method is frequently used to simulate flow in complex structures but can also be used for diffusion simulations under various boundary conditions [30–32].

Here we present an imaging and analysis workflow for the quantitative multiscale characterization of a 2-μm sized porous silica microsphere with 10 nm pores via LC-STEM tomography. The obtained 3D data is used to investigate local variations in pore size distribution, porosity as well as the intraparticle diffusivity and tortuosity of the microsphere via lattice Boltzmann simulations. The results are compared to standard bulk characterization techniques such as nitrogen physisorption and show an excellent match between properties on bulk and single particle level. With this multiscale imaging and quantification workflow at hand, materials that expose hierarchical ordering or a graded porosity can now be investigated.

2. Experimental methods

2.1. Materials

Mesoporous silica microspheres were provided by Nouryon Pulp and Performance Chemicals (Bohus, Sweden) and are commercially available under the brand name Kromasil® Classic - 100 Å SIL 1.8 μm. The material was characterized using nitrogen physisorption (Micromeritics TriStar 3000). The results are shown in Fig. S1. The sample displays IUPAC type IVa behavior, which is characteristic for adsorption behavior inside mesoporous solids. The hysteresis loop indicates a disordered mesostructure. The particles have an average particle size of 2 μm, a BET specific surface area of 317 $m^2\ g^{-1}$, a total pore volume of 0.86 $cm^3\ g^{-1}$, and an average pore diameter of 10.9 nm. The average porosity of the particles was calculated from the total pore volume of the particles and the density of amorphous silicon dioxide [33]:

$$\varphi = \frac{V_{pore}}{\frac{1}{\rho_{SiO2}} + V_{pore}} = 0.65 \quad (1)$$

where V_{pore} is the total pore volume of the particles and ρ_{SiO2} is the density of amorphous SiO_2, which we assume as 2.2 g cm^{-3} [34].

The mesoporous silica microspheres were synthesized according to a method described in detail elsewhere [35]. In brief, the starting material is a basic aqueous silica sol, with a particle size corresponding to an area within the range of from about 50 to about 500 m^2/g. The sol is emulsified in a polar, organic solvent that has a limited miscibility or solubility with water, such as e.g. benzyl alcohol. The emulsification is carried out in the presence of a non-ionic emulsifier, such as cellulose ether. Water from the emulsion droplets is subsequently removed by distillation under an elevated temperature and reduced pressure, causing the silica nanoparticles inside the emulsion droplets to form a gel network. After washing with ethanol and water the silica microspheres are calcined at 600 °C to ensure no organic material is left inside the material. The pore dimensions are governed only by the size of the silica sol nanoparticles and reaction conditions [36]. No templating additives are added to guide or otherwise alter the pore structure.

2.2. STEM tilt-series acquisition

LC-STEM micrographs were recorded at the TU/e FEI CryoTitan electron microscope operating at 300 kV in microprobe STEM mode at spot size 9 with an image sampling of 4096 × 4096 pixels. Image magnification was set at 38000× (pixel size 0.716 nm·px^{-1}), such that only one particle was located in the field of view. The convergence semi-angle was set at 2 mrad and the camera length of the annular dark-field detector (a Fischione HAADF STEM detector) was set to 240 mm. The convergence angle and camera length were experimentally optimized to get a large depth of field as well as to capture as many high-angle scattered electrons as possible, while retaining a high enough spatial resolution to resolve the individual pores. A tilt-series was recorded from a tilt angle of −68° to +68°, every 1° with a total frame time of 20s.

A representative image of the analyzed particles is shown in Fig. S2a. It can clearly be seen that the particle is nearly perfectly spherical.

2.3. Image processing

Most image processing steps were done in MATLAB R2016b using in-house developed code and the DIPlib scientific image processing library V2.8.1. The workflow is shown in Scheme 1 and is further described in the main text. Detailed information regarding each step can be found in the Supplementary Information section 2 and in Figs. S3–S11.

The tomography reconstruction was constructed in IMOD 4.9 using a weighted back projection algorithm with a linear density scaling of 1 and a low-pass radial filter (0.2 px^{-1} cut off with 0.05 px^{-1} fall off) [37]. A median filter (5 × 5 × 5) was applied to remove shot noise. Both filters set the resolution cut-off at 5 pixels.

3D visualization of the reconstruction was done in Avizo 8.1.

2.4. Lattice Boltzmann simulations

In order to transform the tomographic reconstruction into a 3D surface suitable for diffusion simulations, the segmented reconstruction was converted into a triangulated isosurface using VoxSurface 1.2 (VINN Excellence SuMo Biomaterials Center). Lattice Boltzmann simulations were then performed using Gesualdo 1.4 (VINN Excellence SuMo Biomaterials Center). The lattice Boltzmann method was used to solve the diffusion equation using zero flux boundary conditions on the material surface [30]. After the diffusion equation was solved to steady state, the effective diffusion coefficient was computed from the average flux in the direction of the concentration gradient. Additional information can be found in the Supplementary Information section 3.

3. Results and discussion

3.1. Multiscale electron tomography

To image the 3D pore structure of the mesoporous silica microsphere,

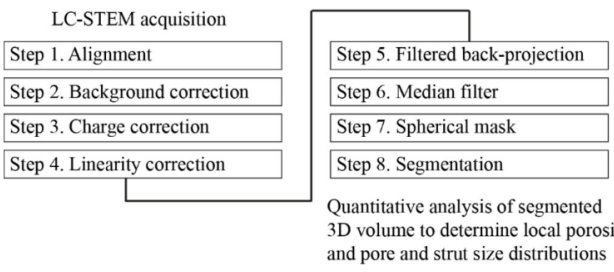

Scheme 1. Workflow for the quantitative electron tomography of a commercial mesoporous silica particle (steps explained in the main text).

a data processing workflow was implemented that is summarized in Scheme 1. The workflow consists of several steps that will be briefly introduced below. For detailed information of each specific step we refer to the Supplementary Information section 2 and supporting Figs. S2–S8.

The first important step towards quantification of an electron tomogram is the alignment of the tilt-series of 2D STEM images (step 1 in Schemes 1 and SI section 2.2.1). Tilt-series alignment is conventionally performed by manual or automatic tracking of the position of several gold fiducial markers on the sample or the support film over each projection angle [37]. However, since the investigated silica particle was close to a perfect sphere, the center of mass of the sphere could be used for tilt-series alignment instead. By tracking the position of the center of mass, the corresponding xy-shifts between images during tilting are obtained. These xy-shifts were subsequently used to align the tilt-series automatically and without the need for any gold fiducial markers.

The intensity of the background with tilt was then corrected (step 2 in Schemes 1 and SI section 2.2.2), followed by the local charging of the particle (step 3 in Schemes 1 and SI section 2.2.3). The silica particle is not interacting uniformly with the electron beam, which causes local charging [38]. Due to this there are two different thickness-intensity relations present in the particle: one for the charged side (left side) and one for the uncharged side (right side) (Fig. 1a). To correct for charging, a mean experimental projection image of the microsphere was calculated. This image was obtained by averaging over all 137 STEM projections using the center 90% percentiles of each pixel. Then, a radial symmetric image of the particle was computed that is based only on the thickness-intensity relation of the non-charged side. By dividing this radial symmetric image by the mean projection image, a correction factor image for the charging effect is obtained. Since the correction factor image is based on the mean projection image, local variations in the porosity of the particle are preserved. After applying the charge correction to the tilt-series, the maximum intensity is observed (as expected for a sphere) in the center of the particle throughout the tilt-series.

To correct for nonlinearity between image intensity and projected thickness (step 4 in Schemes 1 and SI section 2.4.4), a projection of a perfect sphere was created with the same dimensions as the investigated particle. By dividing the projection of a perfect sphere by the mean experimental projection image, a correction factor image for nonlinearity was obtained. Multiplying this correction factor image with the charged corrected images of the tilt-series finally provides an intensity linearized tilt-series of the particle with preserved local variations in porosity (Fig. 1b).

The intensity linearized tilt-series was then reconstructed (step 5 and 6 in Schemes 1 and SI section 2.4.5) by a standard weighted back projection algorithm with linear density scaling [39], a low-pass weighting filter (0.2 px^{-1} cut off with 0.05 px^{-1} fall off) and followed by an edge preserving median filter ($5 \times 5 \times 5$) for further denoising [40]. The reconstruction has a total size of 1601 × 1601 x 1601 voxels and a final pixel size of 1.432 $nm \cdot px^{-1}$. After reconstruction, the 3D data inside a spherical mask corresponding to the particle (step 7 in Schemes 1 and SI section 2.2.6), was segmented using a global intensity threshold (step 8 in Schemes 1 and SI section 2.2.7). This threshold corresponds to a particle porosity of 65%, as determined by N_2 physisorption for the bulk material. Segmentation assigns all pixels with intensities below the threshold to a value of 0 which is considered a pore, while every pixel value above the threshold is set to 1 and considered to be silica. An example of a numerical cross section through the 3D reconstruction is shown in Fig. 1c.

3.2. Quantification of porosity, strut and pore size distributions

Quantification of the segmented reconstruction enables us to calculate globally and locally the porosity, strut and pore size distribution (PSD), which cannot be done by any other means. The segmentation approach that was used to calculate the size distributions is reasonable, because the assumption of a segmentation threshold based on global porosity and the analysis of the local PSDs are not directly related properties.

To quantify the data locally the particle is divided into 13 sub-volumes of 250 × 250 x 250 voxels in size each, which are divided along the x-axis from left to right (in red), along the y-axis from back to front (in green) and along the z-axis from top to bottom (in blue), respectively (Fig. 2a). Size distributions of the pores and struts of respectively the whole particle and of each of the sub-volumes were calculated using the following procedure (Fig. S10). First, a Euclidean distance transform is calculated from the segmented data (inverse logical for pores) to obtain a distance map which, for each point making up the pores, gives the shortest distance between this point to the pore boundary, i.e., the nearest silica surface [41]. Next, the centerlines of the pore network are obtained by skeletonization [42]. By multiplying the distance map with the skeleton of the pore network only values along the centerlines of the pore network are selected and considered for calculation of the pore diameter distribution. Since the values given in the distance map effectively represent the locally observed pore radius, multiplying them by two times the pixel size gives the pore diameter. Due to resolution constraints (reconstruction, noise removal, etc.) values larger than 5 pixels (7.2 nm) are considered reliable. All remaining values are sorted in a histogram with a bin size of 1 pixel (1.4 nm) and normalized with respect to the total pore volume. The same is done for

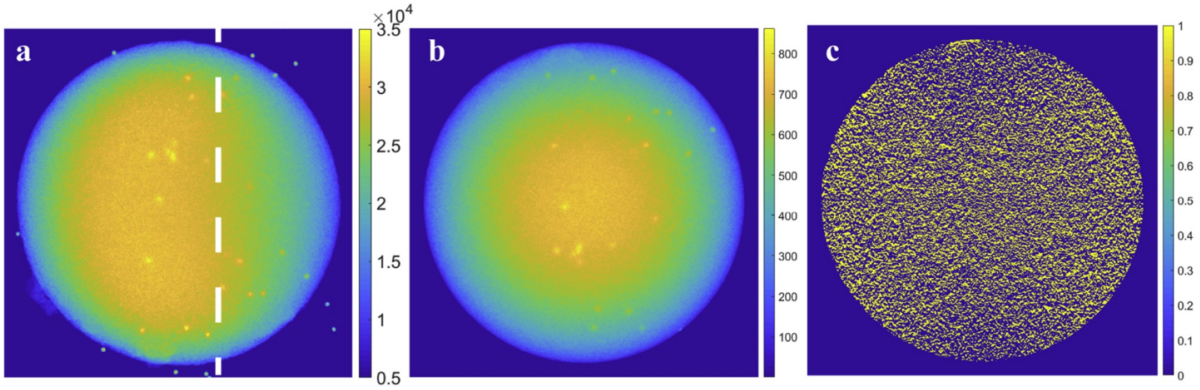

Fig. 1. (a) STEM micrograph at 0° tilt rendered in false color for better visibility of nonlinear thickness and residual charging artifacts. (b) STEM micrograph at 0° tilt after correcting for the background, charge and nonlinearity. The intensity now scales linearly with the thickness. (c) Central numerical cross section after segmentation. The vaguely visible horizontal line through the center is an artefact of the rotation axis. (For interpretation of the references to color in this figure legend, the reader is referred to the Web version of this article.)

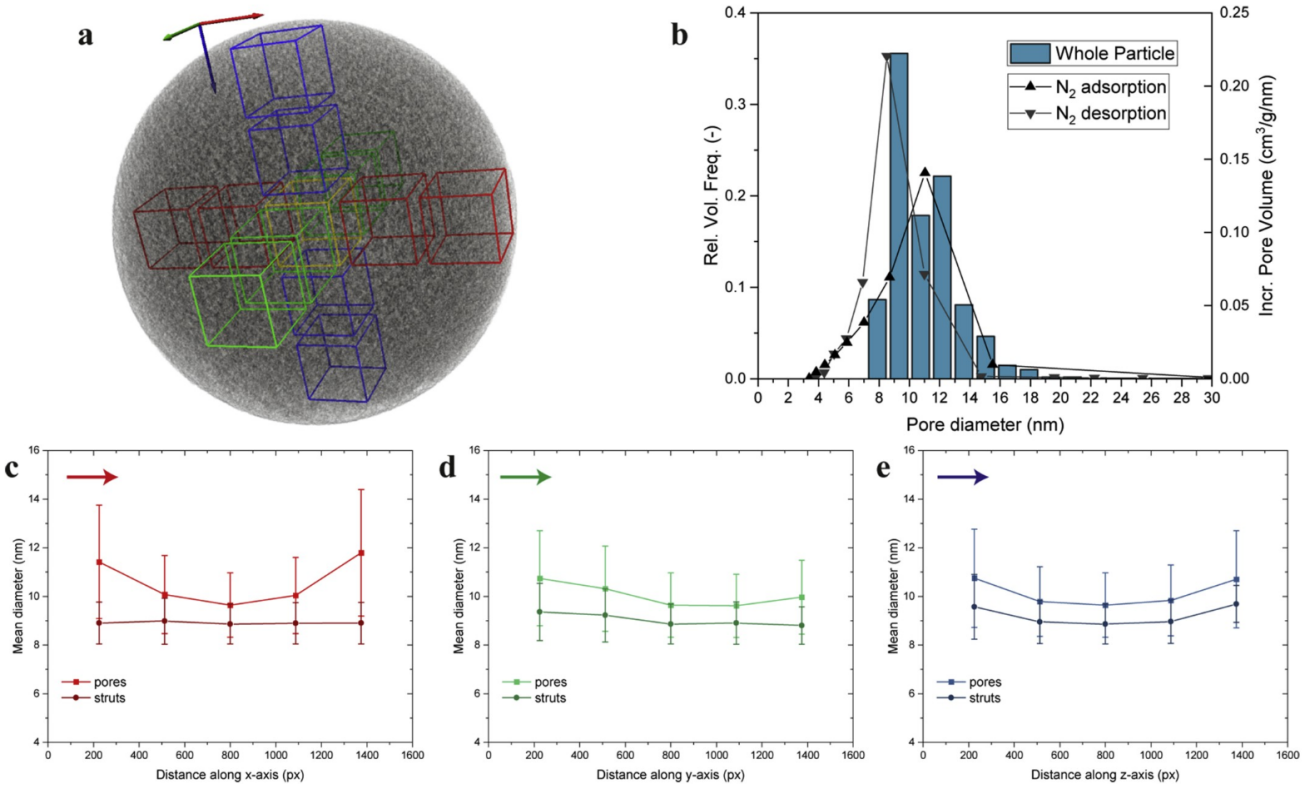

Fig. 2. (a) Schematic representation of the segmented reconstruction in which 13 sub-volumes of 250 × 250 x 250 voxels are highlighted along the x-axis (in red), y-axis (in green), and z-axis (in blue), respectively. (b) Comparison of the PSD of the whole particle as determined via tomography vs the PSD determined via N_2 gas physisorption. The close match indicates an extraordinary particle-to-particle homogeneity. (c–e) Local variations in the mean pore diameter and mean strut diameter along the x-axis, y-axis, and z-axis, respectively. (For interpretation of the references to color in this figure legend, the reader is referred to the Web version of this article.)

the silica strut network using the original binarized data without logical inversion.

Globally, the PSD obtained from the tomography of the whole particle match excellently with the PSD obtained from nitrogen physisorption data on the bulk (Fig. 2b). This indicates an extraordinary homogeneity of the product (from particle to particle). There is a slight difference between the PSD obtained from the adsorption isotherm compared to the desorption isotherm because there is a physical difference in the way the pores are filled (capillary condensation) and emptied (capillary evaporation) [43].

Locally, the PSDs in the middle of the particle are slightly narrower than the PSD over the whole particle and the PSDs on the edge of the particle are slightly broader (Fig. S11). Along the x-axis the pores are somewhat smaller at the center (9.6 ± 1.3 nm) than at the edge of the particle (11.6 ± 2.5 nm), whereas the size of the silica struts network remains constant throughout the particle (8.9 ± 0.9 nm) (Fig. 2c). A similar trend can be seen along the z-axis, except here the size of the silica struts is also slightly larger at the edge of the particle (9.6 ± 1.4 nm) than at the center (Fig. 2d). The sub-volumes along the y-axis show a different trend. Here, the pores are slightly larger at one edge of the particle (10.7 ± 2.0 nm) than at the other edge of the particle (10.0 ± 1.5 nm) (Fig. 2e).

The local porosity, defined as the number of pore pixels times the pixel size and divided over the total size of the sub-volume, also varies slightly throughout the particle. Along the x-axis the porosity is clearly higher at the edge of the particle ($\varphi = 0.74$) compared to the center ($\varphi = 0.62$), whereas it remains relatively constant ($\varphi = 0.62 \pm 0.02$) along the y-axis and z-axis, respectively (Fig. 3a–c). The trend in porosity follows the average pore and strut size variations along the major axis.

Since the pore network of the investigated particle is governed only by the size of the silica sol nanoparticles, and the size of the silica struts network remains constant throughout the particle, the observed inhomogeneity in porosity and pore size must be a result of the formation mechanism. We hypothesize that, due to evaporation of water, the emulsion droplet initially decreases in diameter accompanied by an increase in solid concentration near the droplet interface. This results in gelation starting from the droplet surface with further water evaporation being then somewhat hindered, which could explain a slight difference in particle volume fraction throughout the particle. Similar effects have been observed in, e.g., spray drying of droplets containing solid nanoparticles [44].

These local intraparticle differences indicate subtle but unmistaken local inhomogeneity throughout the particle, which could have a profound impact on the mass transport behavior throughout the particle [45]. This is important because the particle is used in chromatography applications where mass transport plays an important role in the separation efficiency. Insight in the behavior of mass transport through multiscale porous structures can ultimately lead to better computer models and the design of more efficient particles [46].

3.3. Lattice Boltzmann diffusion simulations

The segmented 3D tomography data can also be used to simulate locally the effective diffusion throughout the particle. To do so, the lattice Boltzmann method was used to solve the diffusion equation inside the reconstructed data (SI section 3.1) [31]. This gives a value for the effective intraparticle diffusion coefficient D_{eff} over the free diffusion constant D_0, which depend on the geometry of the structure (porosity and tortuosity) but not on the length scale of the pores (Fig. 3a–c) [47, 48]:

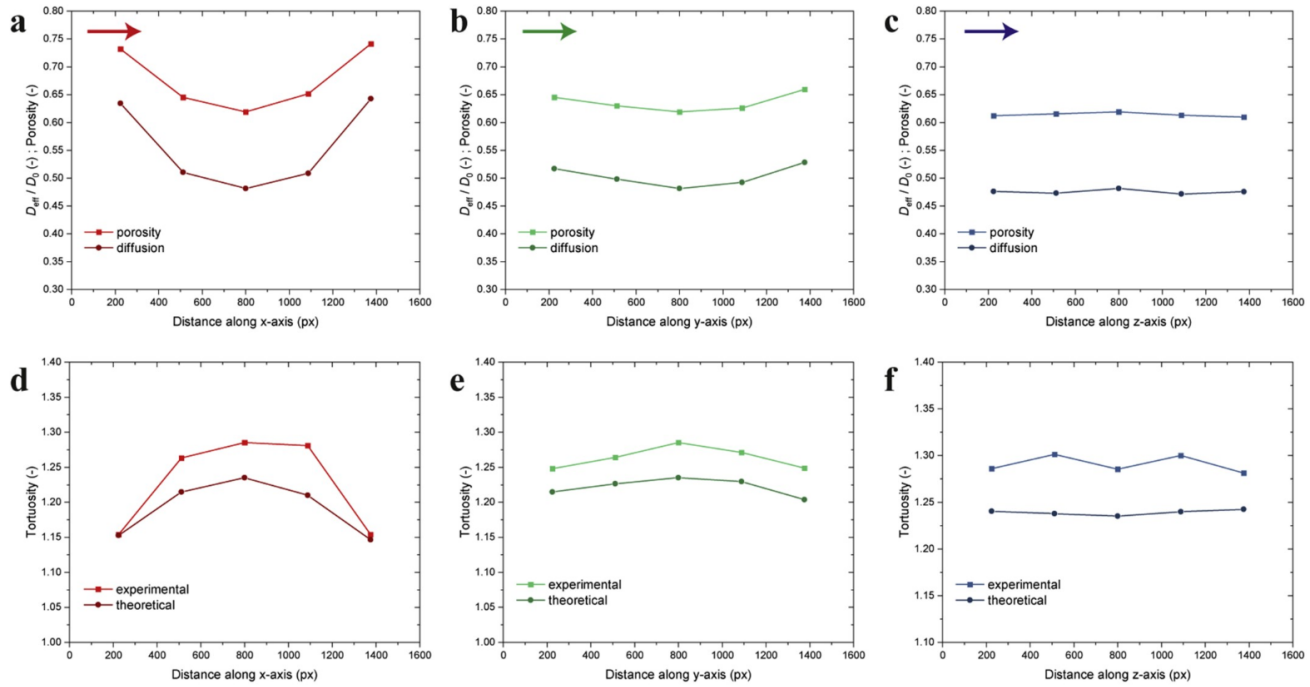

Fig. 3. (a–c) Local variations in the porosity and intraparticle diffusion coefficient along the x-axis, y-axis, and z-axis, respectively. (d–f) Local variations in the intraparticle tortuosity coefficient along the x-axis, y-axis, and z-axis, respectively.

$$D_{eff} = k^* D_0 \quad (2)$$

where D_{eff} is the effect diffusion coefficient in the pore network, D_0 is the free diffusion coefficient (2.3×10^{-9} m^2 s^{-1}) and k^* is a dimensionless proportionality factor called the 'geometry factor'.

The results in Fig. 3a–c show that the diffusion constant is almost proportional to the local particle porosity for each of the three major axis. The higher the local porosity, the higher the local diffusion constant. The diffusion constant was computed in three directions for each individual sub-volume. Although the diffusion coefficient should be more or less constant in each direction because there is no obvious distinct anisotropy in the particle, there is a clear distinction between the diffusion values in the x-,y-, and z-direction in each individual sub-volume (Fig. S12). This is unrelated to the particle structure but is rather a result of the so called 'missing wedge of data' from the tomography due to the limited amount of projection angles [49]. To account for the anisotropic resolution, tomography data was simulated from a perfectly isotropic cube with the same dimensions and porosity as the investigated particle (SI section 3.2). Projections were computed over the experimental angular range (±68°) as well as over the full angular range (±90°). Simulated reconstructions were then calculated with and without the same processing steps that were applied to the experimental tomogram of the investigated particle (Table S1).

The results show that there is no difference in the values for D_{eff}/D_0 with or without processing, indicating that the processing steps that were applied do not shift the location of the pore boundaries. In addition, there is no variation for D_{eff}/D_0 in the x-, y-, and z-direction in each sub-volume when projections were computed over the full angular range. This indicates that anisotropy in the direction of the missing wedge artefact (z-direction) is a limitation of the imaging approach and is unrelated to the observed local inhomogeneity of the investigated particle.

3.4. Intraparticle tortuosity

The relationship between the intraparticle porosity and intraparticle tortuosity, defined as the length of the traveled distance through the medium to the straight-line length across the medium, has significant implications for mass transfer behavior through porous media and has been the subject of many studies over the past decades [50–54]. Barrande et al. [52] derived the following equation for the intraparticle tortuosity from particle conductivity experiments on spherical glass beads:

$$\tau = 1 - 0.49 \ln \varphi \quad (3)$$

where τ is the intraparticle tortuosity and φ is the intraparticle porosity.

Barrande et al. state that tortuosity is a topological characteristic of the material and therefore depends only on porosity for a random system of spheres. As a consequence, they argue that the equation is also valid for any particle that itself is made of a random distribution of dense spheres if the porosity is homogeneously distributed through the particles. Applying Equation (3) on our data and averaging over each of the 15 sub-volumes yields an intraparticle tortuosity of 1.21 ± 0.03 (Fig. 3d–f), which is in good agreement with results reported in literature [52,55]. An intraparticle tortuosity close to 1 indicates that there is little to no hindrance to diffusion, which is important in separation applications [51].

The tortuosity can also be derived from the lattice Boltzmann diffusion simulations [56]:

$$D_{eff} = \frac{\varphi}{\tau} D_0 \quad (4)$$

where φ is the intraparticle porosity and τ is the tortuosity of the structure, D_{eff} is the effective diffusion constant and D_0 is the free diffusion constant.

Applying Equation (4) on our data and averaging over each of the 15 sub-volumes yields an intraparticle tortuosity of 1.26 ± 0.05 (Fig. 3d–f), which is in very good agreement with the intraparticle tortuosity derived from Equation (3). This indicates that Equation (3) is a simple yet surprisingly accurate way to get an indication for the intraparticle tortuosity for these kinds of materials.

The diffusion simulations and tortuosity calculations confirm that

there are local intraparticle differences that will have an impact on the diffusion path across the particle. With these new insights into the intraparticle morphology, steps can be taken towards elucidating the mass transfer behavior inside the studied commercial mesoporous silica microspheres or other materials in the future.

4. Conclusions

We present a method to obtain quantitative local insight into pore and strut size distributions of mesoporous silica spheres and, hence, mass transport through multiscale porous structures using LC-STEM tomography in combination with lattice Boltzmann simulations. We show for the first-time on the example of commercially available mesoporous silica an excellent match between the single microsphere level and the bulk material. Furthermore, quantifying local differences in the pore distribution as well as intraparticle diffusivity and tortuosity that cannot be obtained otherwise highlight the benefits of using multiscale electron tomography in combination with image analysis. Expanding the technique to other materials can lead to new approaches to tune particle porosity and/or graded porosity and to optimize mass transfer kinetics on the single microsphere level.

Funding

This project has received funding from the European Union's Horizon 2020 research and innovation programme under the Marie Skłodowska-Curie grant agreement No 676045 and from a seed-grant from SuMo Biomaterials, a VINN Excellence Center funded by Vinnova.

Declaration of competing interest

The authors declare that they have no known competing financial interests or personal relationships that could have appeared to influence the work reported in this paper.

CRediT authorship contribution statement

Andreas J. Fijneman: Investigation, Writing - original draft, Formal analysis, Visualization. **Maurits Goudzwaard:** Software, Validation. **Arthur D.A. Keizer:** Software, Validation. **Paul H.H. Bomans:** Investigation. **Tobias Gebäck:** Software, Validation, Formal analysis, Writing - review & editing. **Magnus Palmlöf:** Conceptualization, Supervision. **Michael Persson:** Conceptualization, Supervision. **Joakim Högblom:** Conceptualization, Supervision. **Gijsbertus de With:** Writing - review & editing. **Heiner Friedrich:** Conceptualization, Supervision, Investigation, Formal analysis, Visualization, Software, Validation, Writing - review & editing.

Acknowledgements

Electron microscopy was performed at the Center for Multiscale Electron Microscopy, Eindhoven University of Technology. N_2 physisorption experiments were performed at the chemical analysis lab of Nouryon Pulp and Performance Chemicals AB. Lattice Boltzmann simulations were performed at SuMo Biomaterials, VINN Excellence Center, Chalmers University of Technology.

Appendix A. Supplementary data

Supplementary data to this article can be found online at https://doi.org/10.1016/j.micromeso.2020.110243.

References

[1] M.W. Anderson, T. Ohsuna, Y. Sakamoto, Z. Liu, A. Carlsson, O. Terasaki, Modern microscopy methods for the structural study of porous materials, Chem. Commun. 4 (2004) 907–916, https://doi.org/10.1039/b313208k.
[2] B.F. McEwen, M. Marko, The emergence of electron tomography as an important tool for investigating cellular ultrastructure, J. Histochem. Cytochem. 49 (2001) 553–564, https://doi.org/10.1177/002215540104900502.
[3] C. Kübel, A. Voigt, R. Schoenmakers, M. Otten, D. Su, T.C. Lee, A. Carlsson, J. Bradley, Recent advances in electron tomography: TEM and HAADF-STEM tomography for materials science and semiconductor applications, Microsc. Microanal. 11 (2005) 378–400, https://doi.org/10.1017/S1431927605050361.
[4] P.A. Midgley, E.P.W. Ward, A.B. Hungría, J.M. Thomas, Nanotomography in the chemical, biological and materials sciences, Chem. Soc. Rev. 36 (2007) 1477–1494, https://doi.org/10.1039/b701569k.
[5] K.J. Batenburg, S. Bals, J. Sijbers, C. Kübel, P.A. Midgley, J.C. Hernandez, U. Kaiser, E.R. Encina, E.A. Coronado, G. van Tendeloo, 3D imaging of nanomaterials by discrete tomography, Ultramicroscopy 109 (2009) 730–740, https://doi.org/10.1016/j.ultramic.2009.01.009.
[6] Z. Saghi, P.A. Midgley, Electron tomography in the (S)TEM: from nanoscale morphological analysis to 3D atomic imaging, Annu. Rev. Mater. Res. 42 (2012) 59–79, https://doi.org/10.1146/annurev-matsci-070511-155019.
[7] J.E. Evans, H. Friedrich, Advanced tomography techniques for inorganic, organic, and biological materials, MRS Bull. 41 (2016) 516–521, https://doi.org/10.1557/mrs.2016.134.
[8] H. Friedrich, P.E. de Jongh, A.J. Verkleij, K.P. de Jong, Electron tomography for heterogeneous catalysts and related nanostructured materials, Chem. Rev. 109 (2009) 1613–1629, https://doi.org/10.1021/cr800434t.
[9] E. Biermans, L. Molina, K.J. Batenburg, S. Bals, G. van Tendeloo, Measuring porosity at the nanoscale by quantitative electron tomography, Nano Lett. 10 (2010) 5014–5019, https://doi.org/10.1021/nl103172r.
[10] Y. Yao, K.J. Czymmek, R. Pazhianur, A.M. Lenhoff, Three-dimensional pore structure of chromatographic adsorbents from electron tomography, Langmuir 22 (2006) 11148–11157, https://doi.org/10.1021/la0613225.
[11] J. Zečević, K.P. de Jong, P.E. de Jongh, Progress in electron tomography to assess the 3D nanostructure of catalysts, Curr. Opin. Solid State Mater. Sci. 17 (2013) 115–125, https://doi.org/10.1016/j.cossms.2013.04.002.
[12] Y. Sakamoto, M. Kaneda, O. Terasaki, D.Y. Zhao, J.M. Kim, G. Stucky, H.J. Shin, R. Ryoo, Direct imaging of the pores and cages of three-dimensional mesoporous materials, Nature 408 (2000) 449–453, https://doi.org/10.1038/35044040.
[13] M. Kruk, M. Jaroniec, Y. Sakamoto, O. Terasaki, R. Ryoo, C.H. Ko, Determination of pore size and pore wall structure of MCM-41 by using nitrogen adsorption, transmission electron microscopy, and X-ray diffraction, J. Phys. Chem. B 104 (2000) 292–301, https://doi.org/10.1021/jp992718a.
[14] L.R. Snyder, J.J. Kirkland, J.W. Dolan, Introduction to Modern Liquid Chromatography, John Wiley & Sons, Inc., Hoboken, NJ, USA, 2009, https://doi.org/10.1002/9780470508183.
[15] F. Gritti, G. Guiochon, Importance of sample intraparticle diffusivity in investigations of the mass transfer mechanism in liquid chromatography, AIChE J. 57 (2011) 346–358, https://doi.org/10.1002/aic.12280.
[16] F. Gritti, K. Horvath, G. Guiochon, How changing the particle structure can speed up protein mass transfer kinetics in liquid chromatography, J. Chromatogr., A 1263 (2012) 84–98, https://doi.org/10.1016/j.chroma.2012.09.030.
[17] J. Mayer, L.A. Giannuzzi, T. Kamino, J. Michael, TEM sample preparation and damage, MRS Bull. 32 (2007) 400–407, https://doi.org/10.1557/mrs2007.63.
[18] T.F. Johnson, J.J. Bailey, F. Iacoviello, J.H. Welsh, P.R. Levison, P.R. Shearing, D. G. Bracewell, Three dimensional characterisation of chromatography bead internal structure using X-ray computed tomography and focused ion beam microscopy, J. Chromatogr., A 1566 (2018) 79–88, https://doi.org/10.1016/j.chroma.2018.06.054.
[19] E. Maire, J.Y. Buffière, L. Salvo, J.J. Blandin, W. Ludwig, J.M. Létang, On the application of X-ray microtomography in the field of materials science, Adv. Eng. Mater. 3 (2001) 539, https://doi.org/10.1002/1527-2648(200108)3:8<539:AID-ADEM539>3.0.CO;2-6.
[20] J. Loos, E. Sourty, K. Lu, B. Freitag, D. Tang, D. Wall, Electron tomography on micrometer-thick specimens with nanometer resolution, Nano Lett. 9 (2009) 1704–1708, https://doi.org/10.1021/nl900395g.
[21] J. Biskupek, J. Leschner, P. Walther, U. Kaiser, Optimization of STEM tomography acquisition - a comparison of convergent beam and parallel beam STEM tomography, Ultramicroscopy 110 (2010) 1231–1237, https://doi.org/10.1016/j.ultramic.2010.05.008.
[22] T. Segal-Peretz, J. Winterstein, M. Doxastakis, A. Ramírez-Hernández, M. Biswas, J. Ren, H.S. Suh, S.B. Darling, J.A. Liddle, J.W. Elam, J.J. de Pablo, N.J. Zaluzec, P. F. Nealey, Characterizing the three-dimensional structure of block copolymers via sequential infiltration synthesis and scanning transmission electron tomography, ACS Nano 9 (2015) 5333–5347, https://doi.org/10.1021/acsnano.5b01013.
[23] K. Gnanasekaran, R. Snel, G. de With, H. Friedrich, Quantitative nanoscopy: tackling sampling limitations in (S)TEM imaging of polymers and composites, Ultramicroscopy 160 (2016) 130–139, https://doi.org/10.1016/j.ultramic.2015.10.004.
[24] S. Bals, R. Kilaas, C. Kisielowski, Nonlinear imaging using annular dark field TEM, Ultramicroscopy 104 (2005) 281–289, https://doi.org/10.1016/j.ultramic.2005.05.004.
[25] W. van den Broek, A. Rosenauer, B. Goris, G.T. Martinez, S. Bals, S. van Aert, D. van Dyck, Correction of non-linear thickness effects in HAADF STEM electron

tomography, Ultramicroscopy 116 (2012) 8–12, https://doi.org/10.1016/j.ultramic.2012.03.005.
[26] R. Gordon, R. Bender, G.T. Herman, Algebraic Reconstruction Techniques (ART) for three-dimensional electron microscopy and X-ray photography, J. Theor. Biol. 29 (1970) 471–481, https://doi.org/10.1016/0022-5193(70)90109-8.
[27] Z. Zhong, R. Aveyard, B. Rieger, S. Bals, W.J. Palenstijn, K.J. Batenburg, Automatic correction of nonlinear damping effects in HAADF–STEM tomography for nanomaterials of discrete compositions, Ultramicroscopy 184 (2018) 57–65, https://doi.org/10.1016/j.ultramic.2017.10.013.
[28] D. Wolf, R. Hübner, T. Niermann, S. Sturm, P. Prete, N. Lovergine, B. Büchner, A. Lubk, Three-dimensional composition and electric potential mapping of III-V core-multishell nanowires by correlative STEM and holographic tomography, Nano Lett. 18 (2018) 4777–4784, https://doi.org/10.1021/acs.nanolett.8b01270.
[29] T. Krüger, H. Kusumaatmaja, A. Kuzmin, O. Shardt, G. Silva, E.M. Viggen, The Lattice Boltzmann Method, Springer International Publishing, Cham, 2017, https://doi.org/10.1007/978-3-319-44649-3.
[30] I. Ginzburg, Equilibrium-type and link-type lattice Boltzmann models for generic advection and anisotropic-dispersion equation, Adv. Water Resour. 28 (2005) 1171–1195, https://doi.org/10.1016/j.advwatres.2005.03.004.
[31] T. Gebäck, M. Marucci, C. Boissier, J. Arnehed, A. Heintz, Investigation of the effect of the tortuous pore structure on water diffusion through a polymer film using lattice Boltzmann simulations, J. Phys. Chem. B 119 (2015) 5220–5227, https://doi.org/10.1021/acs.jpcb.5b01953.
[32] T. Gebäck, A. Heintz, A lattice Boltzmann method for the advection-diffusion equation with neumann boundary conditions, Commun. Comput. Phys. 15 (2014) 487–505, https://doi.org/10.4208/cicp.161112.230713a.
[33] S. Lowell, J.E. Shields, M.A. Thomas, M. Thommes, Other surface area methods. Charact. Porous Solids Powders Surf. Area, Pore Size Density, sixteenth ed., Springer, Dordrecht, 2004, pp. 82–93, https://doi.org/10.1007/978-1-4020-2303-3_6.
[34] R.K. Iler, The Chemistry of Silica, John Wiley & Sons, Inc., New York, 1979.
[35] M. Nyström, W. Herrmann, B. Larsson, Method for Preparation of Silica Particles, US Patent 5.256.386, 1993.
[36] H. Gustafsson, K. Holmberg, Emulsion-based synthesis of porous silica, Adv. Colloid Interface Sci. 247 (2017) 426–434, https://doi.org/10.1016/j.cis.2017.03.002.
[37] J.R. Kremer, D.N. Mastronarde, J.R. McIntosh, Computer visualization of three-dimensional image data using IMOD, J. Struct. Biol. 116 (1996) 71–76, https://doi.org/10.1006/jsbi.1996.0013.
[38] R.F. Egerton, Radiation damage to organic and inorganic specimens in the TEM, Micron 119 (2019) 72–87, https://doi.org/10.1016/j.micron.2019.01.005.
[39] M. Weyland, P. Midgley, Electron tomography, in: Transm. Electron Microsc, Springer, Cham, 2016, pp. 343–376, https://doi.org/10.1007/978-3-319-26651-0_12.
[40] P. van der Heide, X.P. Xu, B.J. Marsh, D. Hanein, N. Volkmann, Efficient automatic noise reduction of electron tomographic reconstructions based on iterative median filtering, J. Struct. Biol. 158 (2007) 196–204, https://doi.org/10.1016/j.jsb.2006.10.030.
[41] P. Danielsson, Euclidean distance mapping, Comput. Graph. Image Process. 14 (1980) 227–248, https://doi.org/10.1016/0146-664X(80)90054-4.
[42] G. Malandain, S. Fernández-Vidal, Euclidean skeletons, image, Vis. Comput. 16 (1998) 317–327, https://doi.org/10.1016/S0262-8856(97)00074-7.
[43] M. Thommes, K. Kaneko, A.V. Neimark, J.P. Olivier, F. Rodriguez-Reinoso, J. Rouquerol, K.S.W. Sing, Physisorption of gases, with special reference to the evaluation of surface area and pore size distribution (IUPAC Technical Report), Pure Appl. Chem. 87 (2015) 1051–1069, https://doi.org/10.1515/pac-2014-1117.
[44] M. Mezhericher, A. Levy, I. Borde, Theoretical models of single droplet drying kinetics: a review, Dry. Technol. 28 (2010) 278–293, https://doi.org/10.1080/07373930903530337.
[45] F. Gritti, G. Guiochon, New insights on mass transfer kinetics in chromatography, AIChE J. 57 (2011) 333–345, https://doi.org/10.1002/aic.12271.
[46] S.T. Sie, R. Krishna, Fundamentals and selection of advanced Fischer–Tropsch reactors, Appl. Catal. A Gen. 186 (1999) 55–70, https://doi.org/10.1016/S0926-860X(99)00164-7.
[47] L. Shen, Z. Chen, Critical review of the impact of tortuosity on diffusion, Chem. Eng. Sci. 62 (2007) 3748–3755, https://doi.org/10.1016/j.ces.2007.03.041.
[48] B. Ghanbarian, A.G. Hunt, R.P. Ewing, M. Sahimi, Tortuosity in porous media: a critical review, Soil Sci. Soc. Am. J. 77 (2013) 1461–1477, https://doi.org/10.2136/sssaj2012.0435.
[49] I. Arslan, J.R. Tong, P.A. Midgley, Reducing the missing wedge: high-resolution dual axis tomography of inorganic materials, Ultramicroscopy 106 (2006) 994–1000, https://doi.org/10.1016/j.ultramic.2006.05.010.
[50] J. Comiti, M. Renaud, A new model for determining mean structure parameters of fixed beds from pressure drop measurements: application to beds packed with parallelepipedal particles, Chem. Eng. Sci. 44 (1989) 1539–1545, https://doi.org/10.1016/0009-2509(89)80031-4.
[51] B.P. Boudreau, The diffusive tortuosity of fine-grained unlithified sediments, Geochem. Cosmochim. Acta 60 (1996) 3139–3142, https://doi.org/10.1016/0016-7037(96)00158-5.
[52] M. Barrande, R. Bouchet, R. Denoyel, Tortuosity of porous particles, Anal. Chem. 79 (2007) 9115–9121, https://doi.org/10.1021/ac071377r.
[53] M. Matyka, A. Khalili, Z. Koza, Tortuosity-porosity relation in porous media flow, Phys. Rev. E. 78 (2008), 026306, https://doi.org/10.1103/PhysRevE.78.026306.
[54] Z. Sun, X. Tang, G. Cheng, Numerical simulation for tortuosity of porous media, Microporous Mesoporous Mater. 173 (2013) 37–42, https://doi.org/10.1016/j.micromeso.2013.01.035.
[55] F. Gritti, G. Guiochon, Effect ofthe surface coverage of C18-bonded silica particles on the obstructive factor and intraparticle diffusion mechanism, Chem. Eng. Sci. 61 (2006) 7636–7650, https://doi.org/10.1016/j.ces.2006.08.070.
[56] H. Iwai, N. Shikazono, T. Matsui, H. Teshima, M. Kishimoto, R. Kishida, D. Hayashi, K. Matsuzaki, D. Kanno, M. Saito, H. Muroyama, K. Eguchi, N. Kasagi, H. Yoshida, Quantification of SOFC anode microstructure based on dual beam FIB-SEM technique, J. Power Sources 195 (2010) 955–961, https://doi.org/10.1016/j.jpowsour.2009.09.005.